Nano Energy 64 (2019) 103929

Contents lists available at ScienceDirect

Nano Energy

journal homepage: www.elsevier.com/locate/nanoen

Full paper

Highly efficient and stable planar heterojunction solar cell based on sputtered and post-selenized Sb_2Se_3 thin film

Rong Tang[a,1], Zhuang-Hao Zheng[a,b,1], Zheng-Hua Su[a,1], Xue-Jin Li[c], Ya-Dong Wei[a], Xiang-Hua Zhang[b], Yong-Qing Fu[d], Jing-Ting Luo[a], Ping Fan[a], Guang-Xing Liang[a,b,*]

[a] Shenzhen Key Laboratory of Advanced Thin Films and Applications, College of Physics and Optoelectronic Engineering, Shenzhen University, Shenzhen, 518060, PR China
[b] Univ Rennes, CNRS, ISCR (Institut des Sciences Chimiques de Rennes) UMR 6226, F-35000, Rennes, France
[c] School of Science and Engineering, The Chinese University of Hong Kong (Shenzhen), Shenzhen, 518060, PR China
[d] Faculty of Engineering and Environment, Northumbria University, Newcastle upon Tyne, NE1 8ST, UK

ARTICLE INFO

Keywords:
Sb_2Se_3
Thin film
Sputtering
Post-selenization
Planar heterojunction

ABSTRACT

Antimony selenide (Sb_2Se_3) is regarded as one of the key alternative absorber materials for conventional thin film solar cells due to its excellent optical and electrical properties. Here, we proposed a Sb_2Se_3 thin film solar cell fabricated using a two-step process magnetron sputtering followed by a post-selenization treatment, which enabled us to optimize the best quality of both the Sb_2Se_3 thin film and the Sb_2Se_3/CdS heterojunction interface. By tuning the selenization parameters, a Sb_2Se_3 thin film solar cell with high efficiency of 6.06% was achieved, the highest reported power conversion efficiency of sputtered Sb_2Se_3 planar heterojunction solar cells. Moreover, our device presented an outstanding open circuit voltage (V_{OC}) of 494 mV which is superior to those reported Sb_2Se_3 solar cells. State and density of defects showed that proper selenization temperature could effectively passivate deep defects for the films and thus improve the device performance.

1. Introduction

Thin film solar cells have made remarkable progress over the past few years as the power conversion efficiencies (PCE) of copper indium gallium selenide (CIGS) and cadmium telluride (CdTe) have reached over 22% [1,2]. However, the scarcity and toxicity of elements in these two solar cell systems could be problematic when it comes to large-area production in industry. Antimony selenide (Sb_2Se_3) is a promising alternative absorber material compared to the conventional thin film solar cells. Due to its outstanding properties such as simple crystal structure, ideal optical band gap (1.1–1.3 eV), high absorption coefficient ($> 10^5\,cm^{-1}$) and considerable carrier mobility (~10 $cm^2V^{-1}s^{-1}$) [3–5], Sb_2Se_3 has been regarded as one of the most attractive absorber candidates for the next-generation thin film solar cells. Nair et al. [6] firstly report Sb_2Se_3 application in photovoltaic devices and generated a relatively low PCE of 0.66%. Sb_2Se_3-based thin film solar cells have been extensively studied since 2014 when Zhou et al. [7] achieved a 2.26% efficiency using a solution process. Thereafter, various techniques were utilized to fabricate Sb_2Se_3-based thin film solar cells. Tang's group extensively explored thermal evaporation method [8–11] and 6% conversion efficiency was achieved for a ZnO/Sb_2Se_3 superstrate configuration [12]. Further, a PCE of 7.6% was reported using vapor transport deposition (VTD) method to prepare highly [221]-oriented Sb_2Se_3 thin film by Wen et al. [13].

Very recently, a PCE as high as 9.2% of Sb_2Se_3 thin film solar cell with a core-shell structure (non-planar heterojunction) was reported by Li et al. [14]. [001]-oriented Sb_2Se_3 nanorod arrays were successfully deposited onto Mo-coated glass using closed spaced sublimation (CSS) technique. A short circuit current density (J_{SC}) over 30 mA/cm^2 has been obtained by effective carrier extractions along the Sb_2Se_3 nanorods. The study demonstrated that the one-dimensional Sb_2Se_3 nanorod arrays do improve the carrier transport, however, the surface roughness of the absorber as well as the space between nanorods have been significantly increased. This generates a potential problem for this structure as there is a risk that the conventional cadmium sulfide (CdS) film would contact the Mo-coated glass substrate, leading to shunt leakage formation and thus degrading the conversion efficiency of the device [14]. As a result, a thin TiO_2 film was introduced to the system by the author to optimize the coverage of CdS, which will undoubtedly, complicate the whole fabrication process of the device. Hence, although

* Corresponding author. Nanyou Road No. 3688, Shenzhen University, Shenzhen, 518060, PR China.
E-mail address: lgx@szu.edu.cn (G.-X. Liang).
[1] Rong Tang, Zhuang-Hao Zheng and Zheng-Hua Su contributed equally.

https://doi.org/10.1016/j.nanoen.2019.103929
Received 15 June 2019; Received in revised form 16 July 2019; Accepted 23 July 2019
Available online 26 July 2019
2211-2855/ © 2019 The Authors. Published by Elsevier Ltd. This is an open access article under the CC BY license (http://creativecommons.org/licenses/BY/4.0/).

the nanorod array structure represents the highest efficiency of all Sb_2Se_3 thin film solar cells by far, further investigation are required to fully understand the effectiveness of this particular configuration. On the other hand, planar heterojunction has been considered as the most appropriate structure for many thin film solar cells with high efficiencies such as CIGS, CdTe, CZTSSe and perovskite solar cell [15–18]. Moreover, given that apart from the reported nanorod array structure [14], all the other Sb_2Se_3 thin film solar cells with high efficiency are based on planar heterojunction configuration. Therefore, it is vital to continue exploring new methods to fabricate high-quality planar heterojunction Sb_2Se_3 thin film solar cells.

Magnetron sputtering is a well-established thin film deposition method that has been extensively used in absorber layer fabrication for CIGS and CZTS solar cells [19,20]. The method has the merits of easy control composition, excellent uniformity and simple experimental setup. Liang et al. [21] reported a PCE of 3.35% made by a radio-frequency (*RF*) magnetron sputtering method. Well-crystallized Sb_2Se_3 thin film was prepared using *in-situ* sputtering technique at an optimized substrate temperature.

In this paper, a two-step process: *RF* magnetron sputtering deposition of amorphous Sb_2Se_3 followed by a post selenization, was employed to achieve the best reported efficiency of sputtered Sb_2Se_3 solar cells. By carefully optimizing the selenization procedure, highly crystallized [211]-oriented Sb_2Se_3 ribbons and the Mo/Sb_2Se_3/CdS/ITO/Ag device with PCE of 6.06% were achieved, which is the highest conversion efficiency of sputtered Sb_2Se_3 planar heterojunction solar cells. Besides, our device also presents a large open circuit voltage (V_{OC}) of 494 mV which is higher than most of reported Sb_2Se_3 thin film solar cell in literatures [4–14,22–24]. We have found that selenization temperature to be the key for the crystallinity, crystal orientation and chemical composition of the Sb_2Se_3 films as well as the Sb_2Se_3/CdS planar heterojunction quality, and thus the conversion efficiency of the final device.

2. Experimental detail

2.1. Deposition of Sb_2Se_3 thin film

Sb_2Se_3 thin films were deposited using radiofrequency (RF) magnetron sputtering deposition system. Sb_2Se_3 powder with high purity (> 99.99%) were ball milled and sintered to prepare a dense Sb_2Se_3 sputtering target. The XRD pattern of the Sb_2Se_3 target is shown in Supplementary Fig. S1. Mo-coated glass substrates were subsequently cleaned in an ultrasonic bath using detergent, ethanol and deionized water before sputtering deposition. The background pressure of the sputtering vacuum chamber was evacuated below 7.0×10^{-4} Pa prior to the deposition. Ar gas flow rate was 40 sccm and the working pressure was kept at 1 Pa during the deposition process. The sputtering power and duration were selected to be 40 W and 90 min, respectively. There was no external heating during the deposition. As a result, amorphous Sb_2Se_3 thin films with good homogeneity were obtained. Post-selenization process was subsequently carried out in order to better control the crystallization of the Sb_2Se_3 films (the details of selenization process will be discussed later).

2.2. Device fabrication

After the deposition and selenization of Sb_2Se_3 thin films, CdS buffer layer was deposited onto the crystallized Sb_2Se_3 films using chemical bath deposition (CBD). ITO window layer was magnetron sputtered after the deposition of CdS. The device surface was scribed into small squares with identical area by knife and Ag electrodes were deposited onto the ITO surface via thermal evaporation to form metallic contact. A substrate configuration of Mo/Sb_2Se_3/CdS/ITO/Ag was assembled for our Sb_2Se_3 solar cells. All the device efficiency characterizations of this work were based on active area of each device (0.15 cm^2).

2.3. Characterization of the Sb_2Se_3 films and devices

X-ray diffraction (XRD, Ultima-iv, CuK_α radiation under operation conditions of 40 kV and 40 mA from 10° to 60°) was utilized to investigate the crystal orientation of the Sb_2Se_3 films. The surface and cross-sectional microstructures of the Sb_2Se_3 films were characterized using a scanning electron microscope (SEM, SUPRA 55) and the chemical compositions of the films were analyzed using an energy dispersive X-ray spectroscope (EDS, BRUKER QUANTAX 200) equipped with the SEM. Transmission electron microscope (TEM) images were taken using a FEI Titan Cubed Themis G2 300 microscope. The sample for TEM imaging was prepared by ablating the thin film device using focused ion beam (FIB, FEI Scios). The band gap of the Sb_2Se_3 film was measured using a LAMBDA 950 UV/VIS/NIR spectrophotometer. Ultraviolet photoelectron spectroscopy (UPS) measurement was performed using a Thermo Fisher ESCALAB 250Xi x-ray photoelectron spectrometer to determine the Fermi level and valance band of the Sb_2Se_3 films. The current density–voltage (*J-V*) curves of the Sb_2Se_3 devices were measured under 100 mW/cm^2 AM 1.5 G light illumination using a class AAA solar simulator at room temperature. The external quantum efficiency (EQE) spectra were measured using a Zolix SCS101 system and a Keithley 2400 source meter. Temperature-dependent V_{OC} measurements were carried out using a Lakeshore 325 temperature controller and the temperatures were swept from 350 K to 120 K in a step of 30 K. During the measurements, the devices were mounted inside a Janis VPF-100 cryostat and cooled with liquid nitrogen. Capacitance-voltage (*C–V*) measurements were conducted at AC amplitude of 30 mV and frequency of 10 kHz under a dark condition at room temperature. The DC bias voltage during the *C–V* measurements was applied from −1 V to 0.3 V. Drive level capacitance profiling (DLCP) measurements were performed with an AC amplitude from 20 mV to 140 mV and a DC bias voltage from −0.2 V to 0.2 V. Temperature-dependent capacitance-frequency (*C-f-T*) measurements were carried out within the frequency range of 1 kHz–10 MHz using the same cryostat and cooling system as mentioned above.

3. Results and discussion

The schematic diagram of the Sb_2Se_3 thin film preparation and the device fabrication is illustrated in Fig. 1. The full experimental details of magnetron sputtering and device fabrication have been provided in Experimental part. Herein, discussion will be mainly focused on the post-selenization step. After carefully controlling the sputtering parameters, amorphous Sb_2Se_3 thin films with high uniformity were obtained. Subsequently, a post selenization process was carried out using a double-chamber vacuum tubular furnace (Fig. 1). The tubular furnace was evacuated to a relatively low background pressure using a mechanical pump before the selenization commenced, after that high purity Ar (> 99.999%) was pumped into the furnace and the working pressure was kept at 5×10^4 Pa during the whole annealing process. 0.25 g of Selenium (Se) powder with high purity (> 99.999%) was kept at 400 °C during the selenization process whilst the temperature on the Sb_2Se_3 thin film side increased from 340 °C to 460 °C in a step of 40 °C. Correspondingly, the samples annealed at different temperatures were denoted as 340-Sb_2Se_3, 380-Sb_2Se_3, 420-Sb_2Se_3 and 460-Sb_2Se_3. The selenization duration was fixed at 20 min for each annealing scenario. Both the selenium temperature and the substrate temperature were raised at a ramping rate of 20 °C/min to the target temperature. The substrate was naturally cooled down to room temperature in the furnace after selenization.

Morphology and crystalline phases of Sb_2Se_3 films annealed at various temperatures were shown in Fig. 2. From the XRD patterns, the overall diffraction peak intensities are increased with selenization temperature, suggesting crystallinity improvement of the Sb_2Se_3 thin films upon annealing. However, the changes of the diffraction peak intensities are quite different, e.g. the (211), (221) and (002) peaks are

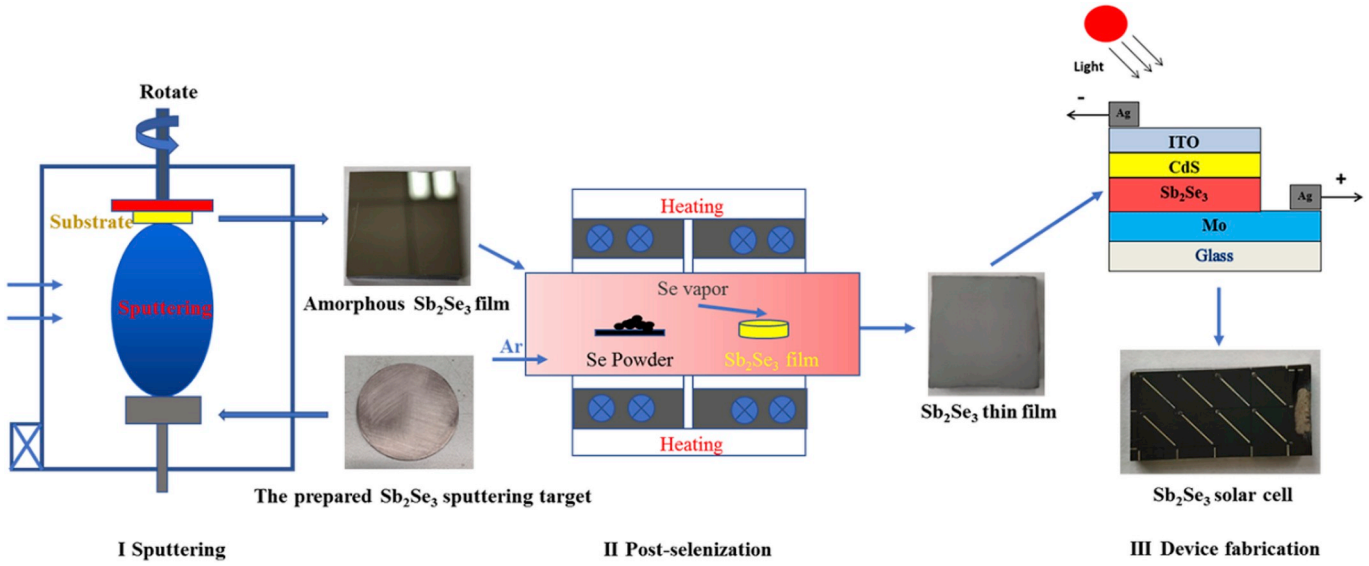


Fig. 1. Schematic of the device fabrication process.

increased sharply with selenization temperature, whereas those of the (120), (230) and (240) peaks decrease when selenization temperature was higher than 380 °C. Film texture has been reported as a key role in control of carrier transport [11]. In order to study the film orientation of Sb_2Se_3 thin films quantitatively, texture coefficients (TC) of the diffraction peaks were calculated (Supplementary Fig. S2) based on the following equation [12]:

$$TChkl = \frac{I(hkl)}{I0(hkl)} / \left(\frac{1}{N}\sum_{i=1}^{N}\frac{I(h_i k_i l_i)}{I0(h_i k_i l_i)}\right) \quad (1)$$

where $I_{(hkl)}$ and $I_{0(hkl)}$ are the diffraction peak intensities of (*hkl*) planes in the measured and standard XRD pattern of Sb_2Se_3 (JCPDS 15–0861), respectively. Large TC value of a diffraction peak indicates preferred orientation along this particular direction [12]. The TC values of (hk0) planes of our samples tend to decrease with increasing selenization temperature in the range of 340–420 °C and then started to increase when the selenization temperature is further increased. Contrarily, the evolution of TC values of planes stacking vertically on the substrate, namely, (211), (221) and (002) planes showed an opposite trend, implying vertical orientation of our Sb_2Se_3 thin film become dominant when the selenization was carried out at 420 °C.

The top-view images of Sb_2Se_3 thin films annealed at different temperatures are shown in Fig. 2a, b, d and e (The surface SEM image of the as-deposited Sb_2Se_3 thin film is given in Supplementary Fig. S3. It is featureless as expected, indicating the as-deposited Sb_2Se_3 thin film is nearly amorphous). When the Sb_2Se_3 film was annealed at 340 °C, the film was slightly crystallized as only tiny grains can be observed on the sample surface. For the sample annealed at 380 °C, larger Sb_2Se_3 grains with size less than 200 nm were formed and distributed evenly over the sample surface. Much larger grains with size over 1 μm can be observed

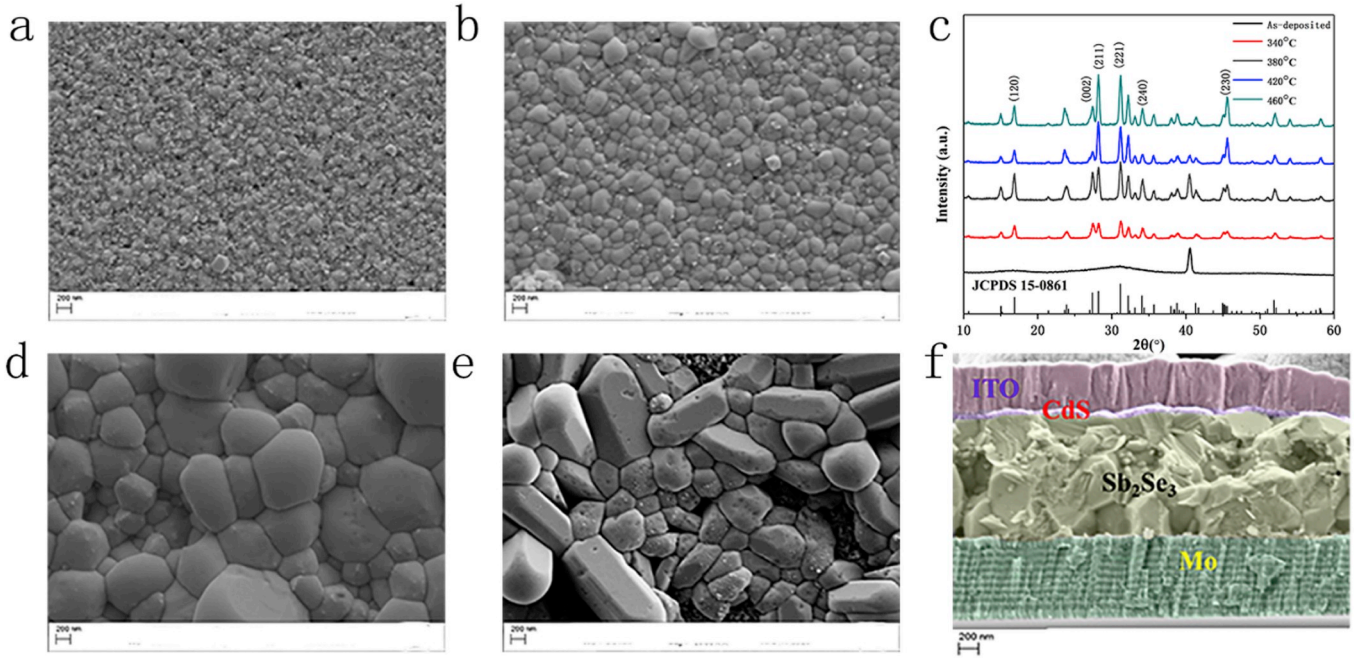


Fig. 2. Morphology evolution of Sb_2Se_3 thin film. SEM top-view images of Sb_2Se_3 thin films annealed at selenization temperatures of 340 °C (**a**), 380 °C (**b**), 420 °C (**d**) and 460 °C (**e**). XRD data of Sb_2Se_3 thin films (**c**). SEM cross-sectional image of Sb_2Se_3 thin film (final device) annealed at 420 °C (**f**).

Table 1
EDS results of Sb_2Se_3 thin films annealed at various temperatures.

Samples	Sb (At%)	Se (At%)	Mo (At%)	Sb/Se
Sb_2Se_3 target	40.34	59.66	N/A	0.676
As-deposited	41.34	57.78	0.88	0.715
340 °C	43.06	55.60	1.34	0.774
380 °C	41.83	56.37	1.80	0.742
420 °C	39.99	58.09	1.92	0.688
460 °C	35.12	57.67	7.21	0.609

on the film surface once the selenization process was conducted at 420 °C. When the selenization temperature was as high as 460 °C, rod-shaped Sb_2Se_3 grains oriented in parallel with the substrate appeared, along with the formation of distinct micro-voids. This is consistent with our XRD data as the texture coefficients of the (hk0) peaks began to increase when selenization temperature was high than 420 °C.

The chemical composition results of the Sb_2Se_3 thin films as well as the sputtering target analyzed by energy dispersive X-ray spectroscopy (EDS) are summarized in Table 1 (EDS patterns of Sb_2Se_3 thin films annealed at various temperatures are shown in Supplementary Fig. S4). Sb_2Se_3 thin films were Se-deficit (the ratios of Sb/Se were significantly higher than the stoichiometric composition of 0.66) when the selenization process was carried out below 400 °C probably due to high vapor pressure of Se. Under these circumstances, selenium vacancy defects could be dominant, affecting the performance of the device. It can be seen that optimal composition of our Sb_2Se_3 thin films with a Sb/Se ratio of 0.688 could be obtained when selenization temperature was 420 °C. Annealing at 460 °C would turn the Sb_2Se_3 film into Se rich as indicated by a Sb/Se ratio of 0.609. However, a high atomic percentage of molybdenum was also detected, suggesting partial decomposition of the thin films due to the excessive temperature. This is consistent with the SEM top-view image (Fig. 2e) as Mo-coated substrate can be directly observed due to the formation of micro-voids.

Overall, selenization temperature plays an important role in fabricating high-quality Sb_2Se_3 films. Sb_2Se_3 thin films prepared by RF magnetron sputtering were found to be optimum in terms of crystallinity, chemical composition and crystal orientation after annealed at 420 °C. Stoichiometric, vertically oriented Sb_2Se_3 grains with size over 1 μm have been successfully prepared under this particular selenization temperature, which is believed to be essential for carrier transport. Improper selenization temperatures would lead to insufficient crystallization or decomposition of the Sb_2Se_3 films, making the films not suitable for device fabrication.

4. Device performance

After the Sb_2Se_3 absorber layer fabrication, CdS, ITO and front electrode were prepared in sequence to make the final device of Mo/Sb_2Se_3/CdS/ITO/Ag in substrate configuration. The cross-sectional image of our complete champion device is displayed in Fig. 2f. Large Sb_2Se_3 grains over 1 μm extending from the substrate to the CdS layer can be directly observed, implying the vertical growth of the Sb_2Se_3 crystals. Decent interfacial adhesion is also evident by the compact and crack-free interfaces between individual layers. The valance band maximum (VBM) and conduction band minimum (CBM) of the Sb_2Se_3 absorber layer that were obtained using ultraviolet photoelectron spectroscopy (UPS) and ultraviolet–visible spectroscopy (*UV-VIS*) techniques are −5.19 eV and −3.98 eV, respectively (Supplementary Fig. S5), whereas the energy levels of CdS and ITO were obtained from the literature [25]. The band alignment diagram of our device is illustrated in Fig. 3a. It can be easily seen that flow of photogenerated electrons from Sb_2Se_3 to ITO could be significantly facilitated due to the optimized band alignment of the device. Besides, considerable VBM

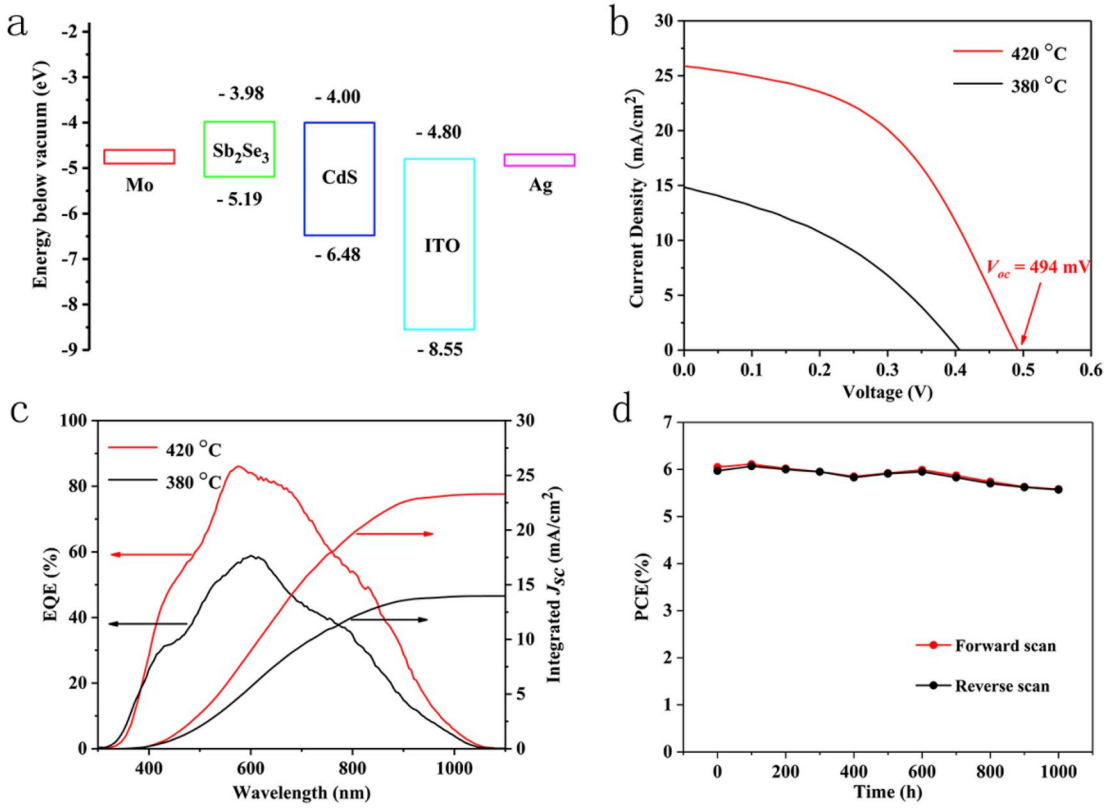


Fig. 3. Device performance. Band alignment diagram of the Sb_2Se_3 device (**a**). Current density-voltage (*J–V*) curves (**b**) and external quantum efficiency (EQE) and integrated J_{SC} (**c**) of 380-Sb_2Se_3 and 420-Sb_2Se_3 devices (**c**). Device stability of the 420-Sb_2Se_3 device after 1000 h storage in air ambient without special treatment/encapsulation (**d**).

offset also makes CdS an effective hole blocking layer which helps to reduce recombination in the device. Since the Sb_2Se_3 films annealed at 340 °C and 460 °C were poorly crystallized and partially decomposed, the devices made from these films barely have any conversion efficiency. Therefore, discussion of device performance will be limited to the 380-Sb_2Se_3 and 420-Sb_2Se_3 devices and the results are shown in Fig. 3b–d.

Device performance tested under AM 1.5 G light illumination showed a PCE of 6.06% for 420-Sb_2Se_3 device, J_{SC} of 25.91 mA/cm^2, V_{OC} of 494 mV and fill factor (*FF*) of 47.73%, whilst the corresponding parameters for the 380-Sb_2Se_3 device are 2.26%, 14.81 mA/cm^2, 407 mV and 38.1%, respectively (Fig. 3b and Supplementary Table S1). 100 devices for each sample category were tested to study the reproducibility of the devices and the main parameter boxplots of the two categories are illustrated in Supplementary Fig. S6. The external quantum efficiency (EQE) of these two devices are given in Fig. 3c, obviously the photo-response of the 420-Sb_2Se_3 device is much stronger than that of the 380-Sb_2Se_3 device over the most of the region. The best device presents EQE values over 80% from 550 to 700 nm, whereas the maximum EQE of the 380-Sb_2Se_3 device is below 60% for the whole region. In summary, the device performance of the 420-Sb_2Se_3 device is superior to that of 380-Sb_2Se_3 device. We attribute this to the optimized orientation and crystallinity of the 420-Sb_2Se_3 thin film. XRD results have demonstrated that annealing at 420 °C significantly induced the growth of vertical oriented grains (mainly [221], [211] and [002] orientation) for the Sb_2Se_3 films, which are believed to have fewer dangling bonds and recombination centers at the grain boundaries [11]. As a result, recombination losses would be minimized and an optimized heterojunction quality could be obtained in the 420-Sb_2Se_3 device. In contrast, Sb_2Se_3 grains have shown orientations in parallel with the substrate surface when annealed at 380 °C and dangling-bond-rich grain boundaries will be produced in this case thus leading to a relatively poor adhesion at the Sb_2Se_3/CdS interface. In addition, much larger grain size in the 420-Sb_2Se_3 device could effectively suppress recombination losses at the grain boundaries further, leading to higher V_{OC} and FF. Moreover, studies have reported that it is much easier for charge carriers to transport through [221] or [211] oriented grains than through [120] oriented grains [11], which is evidenced by the much higher J_{SC} of our 420-Sb_2Se_3 device.

Current density-voltage measurement was also undertaken for our champion device using different scanning directions (Supplementary Fig. S7). A hysteresis-free performance is clearly seen as two curves are overlapped with each other. In order to study the device stability, the device was stored in air ambient without any special treatment/encapsulation for over 1000 h. Device efficiency was tested every 100 h and the result is shown in Fig. 3d. The PCE of our best device was maintained at relatively high levels throughout the whole test and a final PCE of 5.58% (only a small decay of around 9%) was achieved, indicating an excellent stability of our device.

In order to further characterize the morphology and configurational properties of the devices, the champion device was ablated using focused ion beam and cross-sectional TEM image of the device is presented in Fig. 4a. Apparently individual layers including molybdenum substrate, CdS and ITO could be well distinguished. A $MoSe_2$ film could be found between the Mo and Sb_2Se_3 layers which is possibly formed due to high temperature selenization. Such a $MoSe_2$ layer was deliberately introduced into the system prior to Sb_2Se_3 deposition to improve the back contact for Sb_2Se_3 thin film solar cells in substrate configuration, has also been reported by Li et al. [26]. However, the effect of this $MoSe_2$ layer in our case is not fully understand and needs for further investigation. Three arbitrary spots a, b and c were selected for high-resolution transmission electron microscopy (HRTEM) imaging around the top, middle and bottom regions of the Sb_2Se_3 absorber layer to examine the grain continuity across the whole film. Lattice fringes of the three spots are shown in Fig. 4b–d and the distances between lattice lines of all three spots were measured to be 0.318 nm, 0.319 nm and 0.318 nm, respectively. This reveals the excellent continuity of the Sb_2Se_3 grain along the Y-axis direction as all the distances between lattice lines for the three spots are identical which correspond to the (211) planes in orthorhombic Sb_2Se_3. The high consistency of crystal orientation across the whole Sb_2Se_3 film is beneficial for charge carrier transport and thus efficiency improvement [11].

High-angle annular dark-field scanning transmission electron microscope (HAADF-STEM) equipped with energy dispersive spectroscopy (EDS) characterization was further carried out to study the elemental distribution of the device. The red arrow in Fig. 4a indicates the EDS line scan direction. Elemental profiles and elemental mapping of the device are illustrated in Fig. 4e and f, respectively. Elemental

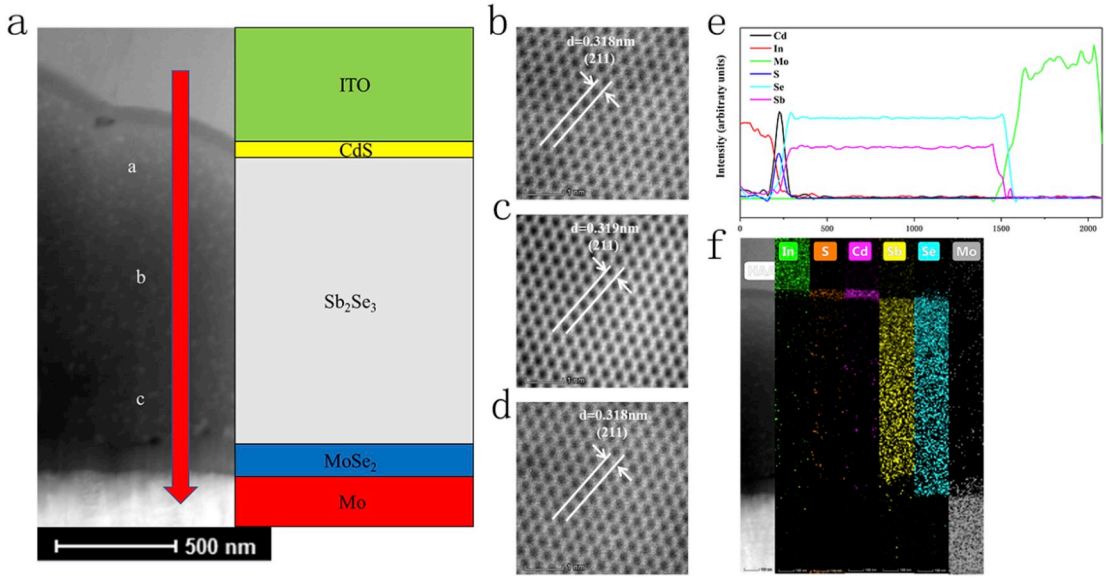


Fig. 4. TEM characterization of the Sb_2Se_3 champion device. Cross-sectional TEM image of the Sb_2Se_3 champion device. The red arrow indicates the EDS line scan direction of the elemental mapping for the device (**a**) Lattice fringes of three arbitrary spots a, b and c across the Sb_2Se_3 thin film in (**a**) performed by HRTEM are given in (**b**), (**c**) and (**d**), correspondingly. EDS elemental profiles (**e**), HAADF-STEM image and EDS elemental mapping (**f**) of the device. (For interpretation of the references to colour in this figure legend, the reader is referred to the Web version of this article.)

distribution with good uniformity of Se and Sb could be clearly observed throughout the whole Sb_2Se_3 layer. Crossovers of different elemental distribution profiles were found at both ends of the Sb_2Se_3 layer, implying occurrence of elemental inter-diffusion at both the Mo/Sb_2Se_3 and Sb_2Se_3/CdS junctions. Since heterojunction interfaces between the absorber layer and buffer layer always play a crucial role in device performance for thin film solar cells, here we will focus our discussion on elemental inter-diffusion at the Sb_2Se_3/CdS heterojunction interfaces. HRTEM images as well as EDS elemental mapping of the Sb_2Se_3/CdS interface are presented in Supplementary Fig. S8. No abrupt interfacial boundary is observed between the Sb_2Se_3 and CdS layers (Supplementary Fig. S8(b)), suggesting good adhesion at the heterojunction interface. For EDS elemental mapping results (Supplementary Fig. S8(c)), elemental inter-diffusions can be observed for all the four elements, i.e. Sb, Se, Cd and S. Such elemental inter-diffusion phenomenon was reported to be essential for favorable band alignment formation and reduction of recombination at the heterojunction interfaces [20]. However, on the other hand, Wang et al. reported that a strong interfacial intermixing, especially over-diffusion of Cd might deteriorate the device performance [12]. Therefore, the full effect of elemental inter-diffusion at the heterojunction interface on device performance for thin film solar cells has not been fully understood yet and future investigations are urgently required for this particular area.

Based on literature, efficiency records of planar heterojunction Sb_2Se_3 thin film solar cells fabricated by various techniques are summarized in Table 2. Compared with Liang's report [21], a nearly 3% efficiency improvement for Sb_2Se_3 solar cell prepared by magnetron sputtering has been achieved in this work. More importantly, our best Sb_2Se_3 solar cell with a conversion efficiency of 6.06% via RF magnetron sputtering represents the highest PCE of all sputtered Sb_2Se_3 planar heterojunction solar cells so far. We attribute this to the additional selenization process which not only compensates for the selenium loss during the sputtering process, but also produce better crystallinity and orientation for the Sb_2Se_3 films. It should be also noted that a large value of open circuit voltage V_{OC} of 494 mV has been achieved, which is higher than any other reported pure Sb_2Se_3 thin film solar cell [4–14,22–24], has been provided by our champion device. A decent short circuit current density J_{SC} of 25.91 mA/cm^2 of our device is comparable to that of state of the art Sb_2Se_3 solar cells as well. However, the fill factor (*FF*) of our device (47.7%) is relatively low compared to other representative devices in the table. The poor FF is probably due to the unoptimized interface between the Sb_2Se_3 thin film and Mo contact. As mentioned before, a thick layer of $MoSe_2$ (~200 nm) could be directly observed from the TEM image of the Sb_2Se_3 device (Fig. 4a). Considering the thickness of $MoSe_2$ layer was only several tens of nanometers in other reports that focused on $MoSe_2$ optimization [26], the over thick $MoSe_2$ layer in this work might increase the series resistance R_S of the device, leading to FF attenuation.

5. Interface characterization of devices

In order to analyze the interfacial properties of the devices, temperature-dependent open circuit voltage (V_{OC}-*T*) measurements were carried out from 350 K to 120 K. Activation energy of recombination activity within the devices can be obtained by extrapolating V_{OC} to the *Y*-axis (Fig. 5a) [12]. The obtained valuer of activation energy for the 420-Sb_2Se_3 device is 1.13 eV, which is very close to the band gap of our Sb_2Se_3 films (1.21 eV), whereas the activation energy of the 380-Sb_2Se_3 device is only 1.06 eV. This implies that interfacial recombination is more prominent for the 380-Sb_2Se_3 device than that for 420-Sb_2Se_3 device [12], mainly due to poor adhesion at the Sb_2Se_3/CdS interface originated from dangling-bond-rich grain boundaries of the 380-Sb_2Se_3 device.

Capacitance-voltage (*C–V*) profiling and deep-level capacitance profiling (*DLCP*) were further conducted to characterize interfacial defects of the devices (Fig. 5b). According to literature [13], the interfacial defect density can be derived from the difference between *C–V* measured doping density (N_{C-V}) and *DLCP* measured doping density (N_{DLCP}) where $N_{C\text{-}V}$ represents responses from free carriers, bulk defects and interfacial defects, while N_{DLCP} only reflects responses from free carriers and bulk defects. The plots of $N_{C\text{-}V}$ and N_{DLCP} against the profiling depth *x* can be calculated according to the following equation:

$$\begin{cases} N_{C-V} = \dfrac{-2\varepsilon_{r,n}N_D}{\left(\frac{d(1/C^2)}{dV}\right)qA^2\varepsilon_0\varepsilon_{r,n}\varepsilon_{r,p}N_D + 2\varepsilon_{r,p}} \\ N_{DLCP} = -\dfrac{C_0^3}{2q\varepsilon_0\varepsilon_{r,p}A^2C_1} \\ x = \varepsilon_0\varepsilon_{r,p}A/C_0 \end{cases} \quad (2)$$

where N_D is the doping density of CdS, *A* is the device area, $\varepsilon_{r,n}$ and $\varepsilon_{r,p}$ are the relative permittivity of CdS and Sb_2Se_3, respectively, C_0 and C_1 are two quadratic fitting parameters derived from the *C–V* curves. It can be clearly seen that the difference between $N_{C\text{-}V}$ and N_{DLCP} of the 420-Sb_2Se_3 device is much smaller than that of the 380-Sb_2Se_3 device, suggesting lower defect density and recombination loss at the Sb_2Se_3/CdS interface for the 420-Sb_2Se_3 device. In the region of Sb_2Se_3/CdS heterojunction interface, nearly the whole depletion width (W_d) is located within Sb_2Se_3 layer since the doping density of Sb_2Se_3 is much lower than that of CdS, as a result, the volume to surface ratio is W_d and interfacial defect densities for 420-Sb_2Se_3 and 380-Sb_2Se_3 devices could be calculated as 1.88×10^{11} cm^{-2} and 1.64×10^{12} cm^{-2}, respectively. It should be noted that the interfacial defect density of our best cell is comparable to that of Sb_2Se_3 solar cells with a high efficiency [12], which yields far superior V_{OC} and *FF* compared with the 380-Sb_2Se_3 device.

C^{-2}-*V* curves were also plotted to calculate the built-in voltage (V_{bi}) for the two devices (Fig. 5c). The curves were linearly fitted and the

Table 2
Summary of planar heterojunction Sb_2Se_3 solar cell publications by different fabrication methods.

Method	Device configuration	*Eff* (%)	V_{oc} (mV)	J_{ac} (mA/cm^2)	*FF* (%)	Ref.
Solution	FTO/TiO_2/CdS/Sb_2Se_3/Spiro/Au	3.9	340	27.2	41.9	Chen [27]
Co-eva[a)]	Glass/Mo/Sb_2Se_3/CdS/ZnO/AZO/Ag	4.25	427	17.11	58.15	Mai [26]
RTE[b)]	ITO/CdS/Sb_2Se_3/Au	7.04	413	28.7	59.3	Tang [24]
VTD[c)]	ITO/CdS/Sb_2Se_3/Au	7.6	420	29.9	60.4	Tang [13]
CSS[d)]	FTO/CdS/Sb_2Se_3/Au	6.84	421	28.4	57.1	Tang [28]
CSS[d)]	Glass/Mo/Sb_2Se_3/$Cd_xZn_{1-x}S$/ZnO/ZnO:Al	6.71	403	25.69	64.78	Mai [29]
Sput[e)]	Glass/Mo/Sb_2Se_3/CdS/ZnO/AZO/Ag	3.35	437	15.93	48	Liang [21]
Sput-Se[f)]	Glass/Mo/Sb_2Se_3/CdS/ITO/Ag	6.06	494	25.91	47.7	This work

[a] Co-evaporation.
[b] Rapid thermal evaporation.
[c] Vapor transport deposition.
[d] Closed space sublimation.
[e] Magnetron sputtering deposition.
[f] Magnetron sputtering deposition and post-selenization.

value of V_{bi} were determined from the x-intercept. Compared with the 380-Sb_2Se_3 device, a sharp V_{bi} increase of 179 mV has been observed for the 420-Sb_2Se_3 device, which is attributed to the greatly improved Sb_2Se_3/CdS interface. As mentioned before, the V_{OC} of our best device (494 mV) is one of the highest values among the state of the art Sb_2Se_3 thin film solar cells prepared by different methods. On the other hand, the V_{bi} of our champion device is also higher than those of many highly efficient Sb_2Se_3 devices in literature [5,26,30,31]. Given that the Sb_2Se_3 grain size of 420-Sb_2Se_3 device is comparable to that of Sb_2Se_3 solar cells with top efficiencies [13,32], the remarkable V_{OC} of our Sb_2Se_3 solar cell could be accounted for by optimized heterojunction quality, large built-in voltage and grain size that originated from the post selenization process.

6. Defect characterization of devices

Defect activation energies and density of defects for the devices were investigated by admittance spectroscopy measured in the temperature range of 210–300 K. The temperature-dependent capacitance-frequency (*C-f-T*) spectra of the devices are shown in Fig. 6a. Larger capacitance variation with the decrease of temperature can be observed for the 380-Sb_2Se_3 device, indicating higher defect density for the device since the capacitance reduction is directly related to dielectric freeze-out of defects at lower temperatures [33]. The inflection point for each admittance spectrum is determined by the Arrhenius plot and the inflection point frequency ω_0 of each curve is derived from the angular frequency point ω at the maximum of the $\omega dC/d\omega$ plot. The Arrhenius plot is linearly fitted based on the equation [34]:

$$\omega_0 = 2\pi\nu_0 T^2 \exp\left(\frac{-E_a}{kT}\right) \quad (3)$$

where ν_0 is the attempt-to-escape frequency, ω_0 is the inflection point frequency and E_a is the defect activation energy that represents the average energetic depth of the defect relative to the VBM or CBM [34]. The E_a values derived from the Arrhenius plots are 456 meV and 495 meV for the 420-Sb_2Se_3 and 380-Sb_2Se_3 device, respectively, as shown in Fig. 6b. As mentioned before, EDS results have revealed that all the Sb_2Se_3 thin films prepared in this work are Se deficit apart from the 460-Sb_2Se_3 device (Table 1). It is known that donor defects namely, antimony antisite Sb_{se} and selenium vacancy V_{se} are prone to form under Se deficit condition [35]. Since the defect activation energies of our devices are in good agreement with the theoretical results by first-principle calculation [35], the activation energies of 456 meV and 495 meV can be ascribed to V_{se} and Sb_{se}, respectively. Considering the difference between the two calculated defect activation energies for both devices is relatively small (ΔE_a = 39 meV), it would be difficult to distinguish them from each other in the devices. What's more, given that E_a represents the average value of the defect activation energies within the devices, in practical situation, it is logical to believe that both kinds of defect would be present in devices. Therefore, in our case, we tentatively attribute V_{se} and Sb_{se} to the dominant defect of 420-Sb_2Se_3 and 380-Sb_2Se_3 device, respectively, as the activation energy of Sb_{se} is estimated to be 30 meV higher than that of V_{se}, according to the first-principle calculation [35]. Since defects with higher activation energy are more likely to behave as recombination centers [33], the 380-Sb_2Se_3 device is expected to suffer from larger recombination center population and thus more severe decline of device performance.

The defect density of each device was Gaussian fitted using the Kimerling model [34] based on the following equation:

$$N_t(E(\omega)) = -\frac{V_d}{q\omega}\cdot\frac{dC}{d\omega}\cdot\frac{\omega}{kT} \quad (4)$$

where E is the energetic distance between the defect energy level and the VBM or CBM, V_d is the built-in voltage of the heterojunction, ω is the angular frequency. The defect density spectra of 420-Sb_2Se_3 and 380-Sb_2Se_3 device are plotted in Fig. 6c and d, respectively, and not surprisingly, a larger defect density was obtained for the 380-Sb_2Se_3 device. Based on the above results, we can conclude that the 380-Sb_2Se_3 device possessed a higher population of donor defects, most of which are Sb_{se} antisites with deeper energy levels than V_{se}. A large number of deep defects will act as recombination centers, yielding recombination losses both in the Sb_2Se_3 layer and the heterojunction interface which can significantly degrade the conversion efficiency of the 380-Sb_2Se_3 device. On the other hand, annealing the Sb_2Se_3 thin films under an optimized selenization temperature (420 °C) can effectively passivate deep defects for the device by making the films towards stoichiometric composition. Of course, the contribution of the reduced recombination rate induced by less defects that originated from the proper crystal orientation and crystallinity should not be ruled out as well.

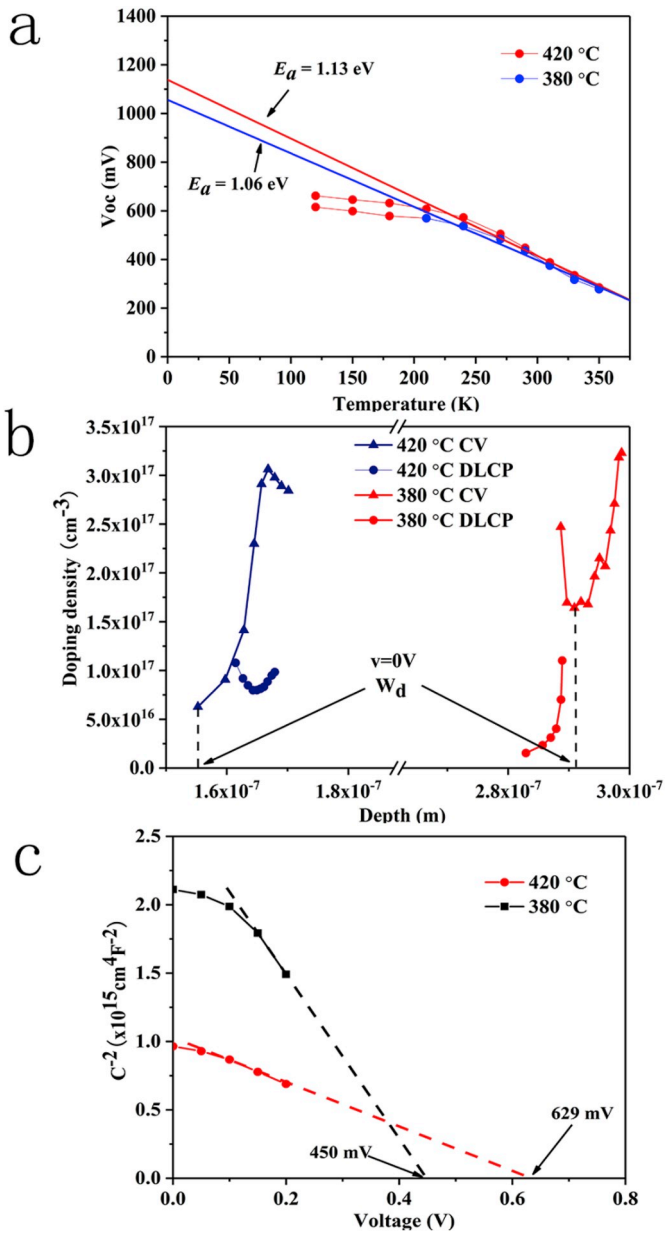


Fig. 5. Sb_2Se_3/CdS interfacial defect characterization of devices. Temperature-dependent open circuit voltage measurements (**a**), *CV* and *DLCP* profiling (**b**), and C^{-2}– V curves (**c**) of 380-Sb_2Se_3 and 420-Sb_2Se_3 devices.

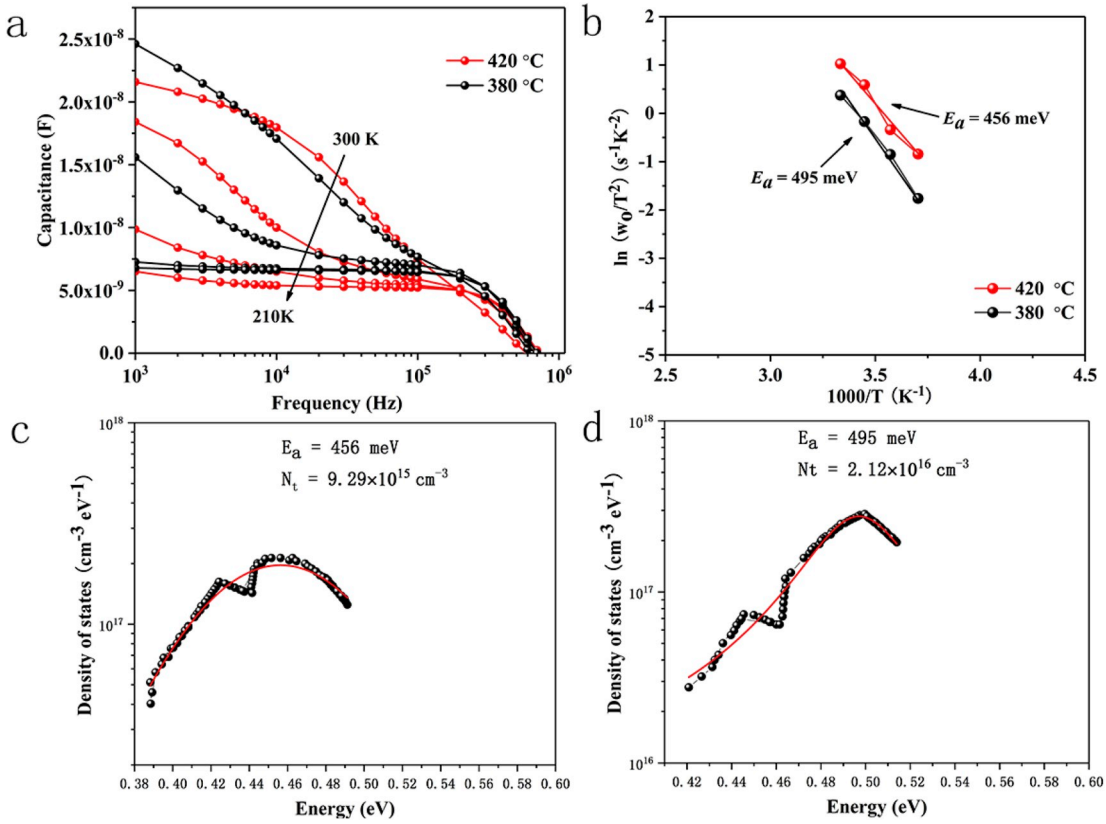


Fig. 6. Temperature-dependent admittance measurements of devices. Capacitance-frequency-temperature (*C-f-T*) spectra (**a**) and defect activation energies (**b**) of the two devices. Defect density spectra of 420-Sb_2Se_3 device (**c**) and 380-Sb_2Se_3 device (**d**) derived from admittance spectra.

7. Conclusions

In summary, we have demonstrated the fabrication of highly efficient and stable Sb_2Se_3 thin film solar cells by magnetron sputtering. A post selenization process was introduced in this work to optimize the Sb_2Se_3 absorber layer in terms of crystallinity, crystal orientation, chemical composition and grain size etc. Selenization temperature is found to be crucial for the Sb_2Se_3 thin film quality. Charge carrier transport optimization, heterojunction interface adhesion improvement as well as defect passivation both in the film and at the interface can be effectively achieved by selecting the proper selenization temperature. After carefully optimizing the selenization process, a final device with a conversion efficiency of 6.06% has been obtained, which represents the highest PCE of sputtered Sb_2Se_3 planar heterojunction solar cells.

Acknowledgment

This work was supported by the Key Project of Department of Education of Guangdong Province (No. 2018KZDXM059), National Natural Science Foundation of China (No. 61404086, U1813207 and 11574217), Shenzhen Key Lab Fund (ZDSYS 20170228105421966). Science and Technology plan project of Shenzhen (JCYJ20180305124340951). The authors wish to acknowledge the assistance on HAADF-STEM observation received from the Electron Microscope Center of the Shenzhen University.

Appendix A. Supplementary data

Supplementary data to this article can be found online at https://doi.org/10.1016/j.nanoen.2019.103929.

References

[1] M.A. Green, et al., Solar cell efficiency tables (version 51), Prog. Photovolt. Res. Appl. 26 (2018) 3–12.
[2] Solar Frontier, Solar Frontier achieves world record thin-film solar cell efficiency of 22.9%. Solar. Frontier, Accessed June 2018, 2017. http://www.solar-frontier.com/eng/news/2017/1220_press.html.
[3] C. Chen, et al., Characterization of basic physical properties of Sb_2Se_3 and its relevance for photovoltaics, Front. Optoelectron. 10 (2017) 18–30.
[4] C. Yuan, et al., Rapid thermal process to fabricate Sb_2Se_3 thin film for solar cell application, Sol. Energy 137 (2016) 256–260.
[5] K. Shen, et al., Mechanisms and modification of nonlinear shunt leakage in Sb_2Se_3 thin film solar cells, Sol. Energy Mater. Sol. Cells 186 (2018) 58–65.
[6] M. Sarah, et al., Antimony selenide absorber thin films in all-chemically deposited solar cells, J. Electrochem. Soc. 156 (2009) H327–H332.
[7] Y. Zhou, et al., Solution-processed antimony selenide heterojunction solar cells, Adv. Energy Mater. 4 (2014) 1079–1083.
[8] X. Liu, et al., Thermal evaporation and characterization of Sb_2Se_3 thin film for substrate Sb_2Se_3/CdS solar cells, ACS Appl. Mater. Interfaces 6 (2014) 10687–10695.
[9] M. Leng, et al., Selenization of Sb_2Se_3 absorber layer: an efficient step to improve device performance of CdS/Sb_2Se_3 solar cells, Appl. Phys. Lett. 105 (2014) 083905.
[10] X. Liu, et al., Improving the performance of Sb_2Se_3 thin film solar cells over 4% by controlled addition of oxygen during film deposition, Prog. Photovolt. Res. Appl. 23 (2015) 1828–1836.
[11] Y. Zhou, et al., Thin-film Sb_2Se_3 photovoltaics with oriented one-dimensional ribbons and benign grain boundaries, Nat. Photonics 9 (2015) 409–415.
[12] L. Wang, et al., Stable 6%-efficient Sb_2Se_3 solar cells with a ZnO buffer layer, Nat. Energy 2 (2017) 17046.
[13] X. Wen, et al., Vapor transport deposition of antimony selenide thin film solar cells with 7.6% efficiency, Nat. Commun. 9 (2018) 2179.
[14] Z.Q. Li, et al., 9.2%-efficient core-shell structured antimony selenide nanorod array solar cells, Nat. Commun. 10 (2019) 125.
[15] A. Chirilă, et al., Potassium-induced surface modification of Cu(In,Ga)Se_2 thin films for high-efficiency solar cells, Nat. Mater. 12 (2013) 1107–1111.
[16] L. Kranz, et al., Doping of polycrystalline CdTe for high-efficiency solar cells on flexible metal foil, Nat. Commun. 4 (2013) 2306.
[17] W. Wang, et al., Device characteristics of CZTSSe thin-film solar cells with 12.6% efficiency, Adv. Energy Mater. 4 (2014) 1301465.
[18] N.J. Jeon, et al., Solvent engineering for high-performance inorganic–organic hybrid perovskite solar cells, Nat. Mater. 13 (2014) 897–903.
[19] J.H. Shi, et al., Fabrication of Cu(In,Ga)Se_2 thin films by sputtering from a single

quaternary chalcogenide target, Prog. Photovolt. Res. Appl. 19 (2) (2011) 160–164.
[20] Chang Yan, et al., Cu_2ZnSnS_4 solar cells with over 10% power conversion efficiency enabled by heterojunction heat treatment, Nature Energy 3 (9) (2018) 764.
[21] G.X. Liang, et al., Thermally induced structural evolution and performance of Sb_2Se_3 films and nanorods prepared by an easy sputtering method, Sol. Energy Mater. Sol. Cells 174 (2018) 263–270.
[22] J.H. Tao, et al., Investigation of electronic transport mechanisms in Sb_2Se_3 thin-film solar cells, Sol. Energy Mater. Sol. Cells 197 (2019) 1–6.
[23] J.H. Tao, et al., Solution-processed SnO_2 interfacial layer for highly efficient Sb_2Se_3 thin film solar cells, Nano Energy 60 (2019) 802–809.
[24] C. Chen, et al., Efficiency improvement of Sb_2Se_3 solar cells via grain boundary inversion, ACS Energy Letters 3 (10) (2018) 2335–2341.
[25] W.H. Wang, et al., Promising $Sb_2(S,Se)_3$ solar cells with high open voltage by application of a TiO_2/CdS double buffer layer, Solar RRL 2 (11) (2018) 1800208.
[26] Z.Q. Li, et al., Sb_2Se_3 thin film solar cells in substrate configuration and the back contact selenization, Sol. Energy Mater. Sol. Cells 161 (2017) 190–196.
[27] X.M. Wang, et al., Interfacial engineering for high efficiency solution processed Sb_2Se_3 solar cell, Sol. Energy Mater. Sol. Cells 189 (2019) 5–10.
[28] D.B. Li, et al., Stable and efficient CdS/Sb_2Se solar cells prepared by scalable close space sublimation, Nano Energy 49 (2018) 346–353.
[29] G. Li, et al., Improvement in Sb2Se3 solar cell efficiency through band Alignment engineering at the buffer/absorber interface, Appl. Mater. Interfaces 11 (2019) 828–834.
[30] X.B. Hu, et al., Improving the efficiency of Sb_2Se_3 thin-film solar cells by post annealing treatment in vacuum condition, Sol. Energy Mater. Sol. Cells 187 (2018) 170–175.
[31] Y. Zhou, et al., Buried homojunction in CdS/Sb_2Se_3 thin film photovoltaics generated by interfacial diffusion, Appl. Phys. Lett. 111 (1) (2017) 013901.
[32] O.S. Hutter, et al., 6.6% efficient antimony selenide solar cells using grain structure control and an organic contact layer, Sol. Energy Mater. Sol. Cells 188 (2018) 177–181.
[33] H.S. Duan, et al., The role of sulfur in solution-processed $Cu_2ZnSn(S,Se)_4$ and its effect on defect properties, Adv. Funct. Mater. 23 (11) (2013) 1466–1471.
[34] J.J. Li, et al., Tailoring the defects and carrier density for beyond 10% efficient CZTSe thin film solar cells, Sol. Energy Mater. Sol. Cells 159 (2017) 447–455.
[35] X.S. Liu, et al., Enhanced Sb_2Se_3 solar cell performance through theory-guided defect control, Prog. Photovolt. Res. Appl. 25 (10) (2017) 861–870.



Guangxing Liang is an associate researcher in College of Physics and Optoelectronic Engineering, Shenzhen University, Shenzhen, China. He obtained his PhD degree from University of Rennes 1, Rennes, France. He has extensive experience in solar energy materials and solar cells, including Sb_2Se_3, CZTS and perovskite, etc. He published over 100 science citation index (SCI) journal papers. He is regular journal paper reviewers for more than 10 journals. He is the academic editors of Advances in Materials Science and Engineering.



Ping Fan is a professor in College of Physics and Optoelectronic Engineering, Shenzhen University, China. He is the director of Shenzhen Key Laboratory of Advanced Thin Films and Applications and Shenzhen Vaccum Society. He received his PHD in Shanghai Institute of optical and Fine Mechanics Chinese Academy of Sciences, China, in 2005. He has published more than 100 SCI papers. His research interests include solar energy materials and solar cells, thermoelectric materials and devices. He is regular journal paper reviewers for more than 20 journals.



Rong Tang received his Ph.D. degree in Pure and Applied Chemistry Department, Faculty of Science, University of Strathclyde, Glasgow, United Kingdom. He works in Shenzhen Key Laboratory of Advanced Thin Films and Applications, College of Physics and Optoelectronic Engineering, Shenzhen University as a postdoctoral researcher. His main research areas are novel materials and Sb_2Se_3 thin film solar cells.



Zhuanghao Zheng received his PhD degree from University of Rennes 1, Rennes, France in 2018. He is an associate researcher in College of Physics and Optoelectronic Engineering, Shenzhen University, Shenzhen, China. His research interests include solar energy materials and solar cells, thermoelectric materials and devices.



Zhenghua Su obtained his PhD degree from Central South University, and then worked as a Research Fellow in Nanyang Technological University, Singapore. Now he is an associate researcher in College of Physics and Optoelectronic Engineering, Shenzhen University, Shenzhen, China. He has extensive experience in semiconductor thin film/materials, thin film solar cells. He published over 40 science citation index (SCI) journal papers and his current SCI H-index is 18.



Xuejin Li received his PhD degree from Tianjin University in Physical Electronics, China. His research mainly focuses on optic fiber sensor technologies and thin-film device. He leads a group at Shenzhen University, and is the directors of Shenzhen Key Laboratory of Sensor Technology and Shenzhen Engineering Laboratory for Optical Fiber Sensors and Networks. He has published more than 120 papers, and applied 24 patens. He was given the honorary titles of the Talent Project of Guangdong Province in 2008 and the Outstanding Scholar of Shenzhen University in 2013.



Yadong Wei received his PhD in the department of physics in the university of Hong Kong. He is now the professor of the college of physics and optoelectronic engineering of Shenzhen university. His main research fields are the theoretical investigations of quantum electron transport, the new material and device first principle calculations, and research on material informatics.



Xianghua Zhang received his PhD degree in chemistry in University of Rennes 1, France. He has been working in the laboratory of glasses and ceramics of the same university for 30 years, now as research director of the CNRS (National center for scientific research). His main research area is on chalcogenide materials for infrared photonics and energy applications. He is author or co-author of more than 300 publications in peer-reviewed journals.



YongQing (Richard) Fu is a professor in University of Northumbria at Newcastle, UK. He obtained his PhD degree from Nanyang Technological University, Singapore, and then worked as a Research Fellow in Singapore-Massachusetts Institute of Technology Alliance, and a Research Associate in University of Cambridge. He has extensive experience in smart thin film/materials, biomedical microdevices, energy materials, lab-on-chip, micromechanics, MEMS, nanotechnology, sensors and microfluidics. He published over 360 science citation index (SCI) journal papers and his current SCI H-index is 45.



Jingting Luo received his PhD degree from Tsinghua University in 2012. From 2012 to 2016 he worked as an assistant professor in College of Physics and Technology in Shenzhen University, Shenzhen, China. He has extensive experience in thin film/materials, nanostructured composite/films and solar cells. He published over 100 science citation index (SCI) journal papers. He is regular journal paper reviewers for more than 10 journals.